Journal Name

ARTICLE TYPE

Cite this: DOI: 10.1039/xxxxxxxxxx

Vibrational Contributions to Intrinsic Friction in Charged Transition Metal Dichalcogenides

Antonio Cammarata,*[a] and Tomas Polcar[a,b]

Received Date
Accepted Date

DOI: 10.1039/xxxxxxxxxx

www.rsc.org/journalname

Vibrational contributions to intrinsic friction in layered transition metal dichalcogenides (TMD) have been studied at different charge content. We find that any deviation from charge neutrality produces complex rearrangements of atomic positions and electronic distribution, and consequent phase transitions. Upon charge injection, cell volume expansion is observed, due to charge accumulation along an axis orthogonal to the layer planes. Such accumulation is accounted by the $d_{3z^2-r^2}$ orbital of the transition metal and it is regulated by the $\mathscr{P}_{t_{2g},e_g}$ orbital polarization. The latter, in turn, determines the frequency of the phonon modes related to the intrisic friction through non-trivial electro-vibrational coupling. The bond covalency and atom pair cophonicity can be exploited as a knob to control such coupling, ruling subtle charge flows through atomic orbitals hence determining vibrational frequencies at specific charge content. The results can be exploited to finely tune vibrational contributions to intrinsic friction in TMD structures, in order to facilitate assembly and operation of nanoelectromechanical systems and, ultimately, to govern electronic charge distribution in TMD-based devices for applications beyond nanoscale tribology.

Introduction

Layered transition metal dichalcogenides (TMDs) attract great technological interests thanks to their highly versatile stoichiometry and their close features with graphene. Production of advanced TMD-based nanostructured materials mainly relies on the comprehension of local frictional forces. Lubricants are able to reduce friction at the macroscopic scale, but assembly and functionality of micro- or nanoelectromechanical systems (NEMS) require a deep knowledge of the mechanisms governing friction at atomic scale. The fundamental processes at the basis of the macroscopic friction have been subject of theoretical and experimental interest in tribology since long time.[1,2] Several attempts to model friction have been done so far,[3] and only a few theoretical studies took into account the explicit atomic structure of the tribological contacts;[4–10] a deep investigation on the electron-phonon coupling effects on the *intrinsic* frictional properties is, however, still required. We call *intrinsic friction* the friction generated by the relative motion of few subsequent atom layers in the absence of structural imperfections (dislocations, layer truncations *etc.*); it then originates from the atomic type and the geometric arrangement of the atoms forming the pristine compound, together with the resulting electronic features. In tribological conditions, non-null net charges can arise[11–14] and redistribute in the neighbourood of the volume where they originated; this corresponds to a charge injection across several layers, and to a perturbation of their charge neutrality. Such perturbation influences the intrinsic frictional properties, the latter being highly relevant in the micromanupulation of free-standing atomic layers,[15] hence in the final design of TMD-based nanostructured materials. Charges may be free to move through the material or may localize in the local environment of specific atomic sites. As a consequence, attractive or repulsive Coulombic forces may arise, either hindering or facilitating relative layer gliding, depending on several factors such as sliding velocity, temperature and atomic types forming the structure. However, these latter aspects are out of the scope of the present study and will be investigated in future works.

In the present manuscript, we will focus on how the presence of non-null charge affects the frequency of the phonon modes which are relevant to the layer sliding phenomenon. The lower the frequency of such modes, the easier the sliding motion, the lower their contribution to the intrinsic friction. This can be understood in terms of the classical picture. At a constant energy of the system, the lower the frequency of a mode, the higher the amplitude of the corresponding atomic displacements; ample displacements, corresponding to relative layer shifts, promote layer sliding. Our goal is to understand which electronic and structural features determine the frequency of such modes and how the presence of

[a] *Department of Control Engineering, Czech Technical University in Prague, Technicka 2, 16627 Prague 6, Czech Republic. Fax: +420 224 91 8646; Tel: +420 224 35 7598; E-mail: cammaant@fel.cvut.cz*
[b] *nCATS, FEE, University of Southampton, SO17 1BJ Southampton, United Kingdom.*

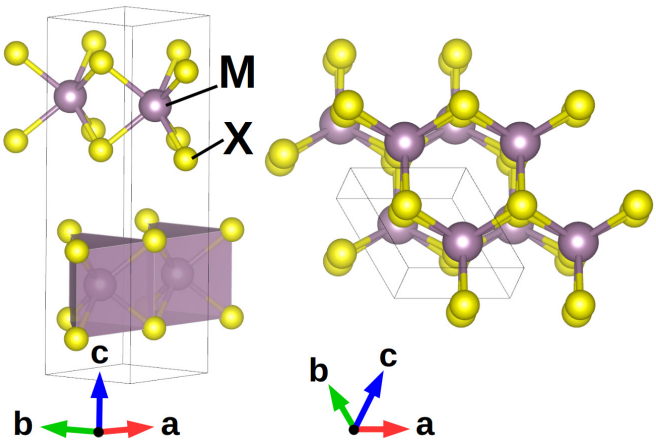

Fig. 1 Model structure of hexagonal $P6_3/mmc$ 2H polymorph of MX_2 TMD crystal. M–X bonds form trigonal prisms arranged in parallel layers which can reciprocally slide thanks to weak van der Waals interactions.

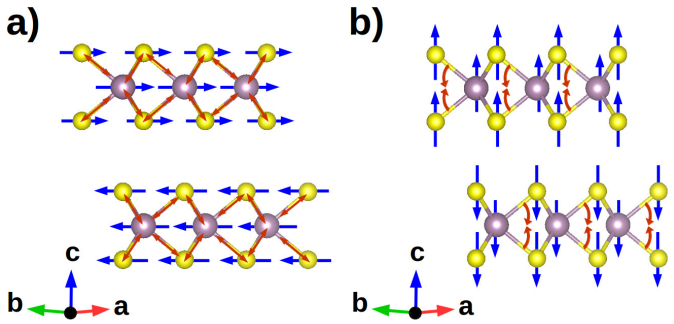

Fig. 2 Schematics of (a) relative layer sliding and (b) out-of-phase vertical shifts. Red arrows indicate eventual intralayer motions which overlap with interlayer displacements (blue arrows). Atom color legend is the same as in Figure 1.

non-null charge influence them; at the same time, we want to learn how to tune such features, in order to find guidance to design new TMDs with enhanced intrinsic frictional response.

We will show that there is no trivial relation between the net charge of the system and the mode frequencies of the latter; however, by exploiting electronic and structural descriptors, we are able to identify guidelines to control subtle features of the electronic density, hence the frequency of the sliding-related phonon modes.

Computational Details

Transition metal dichalcogenides have layered structure with general stoichiometry MX_2, where M is a transition metal and X is a chalcogen. Each MX_2 layer is formed by hexagonally packed metal atoms coordinating six chalcogen anions in a trigonal prismatic fashion (Figure 1); adjacent layers are bound by weak van der Waals forces which allow relative sliding under tribological conditions. Among the several stable TMDs polymorphs and polytypes that are found,[16] we consider $2\times2\times2$ supercells of the 2H polymorph crystalline MX_2 compounds as reference structures, with M=Mo, W and X=S, Se, Te, and hexagonal $P6_3/mmc$ symmetry (SG 194); for simplicity, we will refer to them as MX by dropping the stoichiometric coefficients. The 2H configuration consists of two adjacent layers arranged in such a way that a metal atom of one layer is aligned with two anions of the other one along the direction orthogonal to each layer (c-axis in our setting — see Figure 1).

We perform density functional theory (DFT) calculations using the projector-augmented wave (PAW) formalism and the Perdew-Burke-Ernzerhof (PBE) energy functional[17] as implemented in VASP.[18] We also take into account Van der Waals interactions using the Grimme correction,[19] that is able to reproduce the structural features, as we reported in previous works and references therein.[20–22] The Brillouin zone is sampled with a minimum of a $5\times5\times3$ k-point mesh and plane wave cutoff of 550 eV. We consider neutral as well as charged systems, with charge $q = 0, \pm0.01, \pm0.03 \pm 0.05, \pm0.1, \pm0.2, \pm0.3, \pm0.5, \pm0.7, \pm1.0|e|/\text{cell}$, where one "cell" is a $2\times2\times2$ supercell of the reference unit cell. Full structural (atoms and lattice) relaxations are initiated from diffraction data[23–28] and the forces minimized to a 0.5 meV Å^{-1} tolerance. We computed phonon band structures with the aid of the PHONOPY software.[29]

Results and Discussions

In our previous works,[20–22] we already pointed out how few low-frequency phonon modes are directly connected with the relative sliding of adjacent layers. These consist of relative layer glides and out-of-phase vertical (parallel to $\hat{c}$) shifts of subsequent layers, eventually combined with intralayer motions (Figure 2); we will refer to such modes as *sliding* and *compressive* modes. Following the standard convention, we label them with increasing integers corresponding to dispersion branches with relative increasing frequency; for example, the $\Gamma(5)$ mode is the mode corresponding to the fifth branch at the Γ point of the reciprocal lattice, the frequency of which is higher (or equal in case of degeneracy) than that associated to the $\Gamma(4)$ mode, and lower (or equal) than that relative to the $\Gamma(6)$ mode.

Lattice parameters. We first relax the model geometries and compute the corresponding phonon band structure along a standard[30] path joining the high-symmetry points of the irreducible Brillouin zone (IBZ). We do not find unstable displacements, with the exception of the MoS systems with $q = -0.5, -0.7, -1.0|e|/\text{cell}$; the careful search of the stable states we performed on the latter cases, indeed, suggests that such instabilities cannot be removed unless the charge content is variated. For this reason, we will exclude these cases from our present analysis.

Perturbation of the charge neutrality induces reduction of system symmetries, from hexagonal to orthorhombic, monoclinic or triclinic (Table 1); among the charged systems, we notice that the MoTe, WSe and WTe models maintain the geometry with the highest symmetry ($Cmcm$) at very different charge amounts. This can be qualitatively ascribed to the fact that larger ions can accomodate charge variations better than smaller ones, limiting eventual symmetry reductions.

Table 1 Crystallographic space group of the fully relaxed TMD systems at the considered charge content q ($|e|$/cell). MoS systems with $q = -0.5, -0.7, -1.0|e|$/cell are not considered due to the presence of structural instabilities.

System / q	-1.0	-0.7	-0.5	-0.3	-0.2	-0.1	-0.05	-0.03	-0.01	0.0	0.01	0.03	0.05	0.1	0.2	0.3	0.5	0.7	1.0
MoS	—	—	—	1	6	40	40	40	194	194	194	1	1	63	6	1	5	1	1
MoSe	1	1	1	1	1	1	63	63	194	194	63	63	63	63	2	1	1	1	1
MoTe	63	63	63	63	63	63	63	63	194	194	194	63	63	1	1	1	6	12	12
WS	15	15	1	15	15	15	15	15	194	194	194	63	63	63	1	1	1	2	2
WSe	1	1	1	8	1	1	63	63	194	194	194	63	63	63	63	63	63	63	63
WTe	63	63	63	63	63	63	63	63	194	194	63	63	63	63	63	63	63	63	63

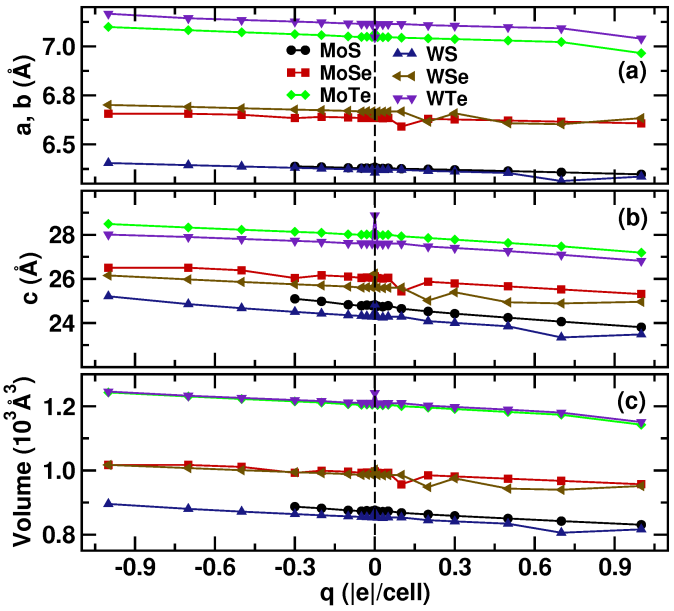

Fig. 3 Lattice parameters (a-b) and volume (c) of the considered MX models as a function of the system charge q. Lines are guides for the eye.

Concerning the lattice vectors, at each MX composition, $a = b$ irrespective of the charge content (Figure 3a); a (b) is globally increasing with increasing q, the variation range being about 0.1 Å. At $q = 0$, a-axis has a local maximum for the MoX compounds, while it has a local minimum for the WX compounds; on the other hand, c-axis has a local maximum at $q = 0$ irrespective of the composition although more pronounced in WX compounds, and its variation range is about 1.5 Å throughout the entire charge range (Figure 3b). The behaviour of crystallographic axes about $q = 0$ indicates that a small perturbation of the charge neutrality is enough to induce structural transitions: at $q = \pm 0.05|e|$/cell, the symmetry is lowered from hexagonal to orthorhombic, monoclinic (WS at $q = -0.05|e|$/cell), or triclinic (MoS at $q = 0.05|e|$/cell). In all the charged systems, at fixed X anion, c-axis is longer when M=Mo. Considering that c-axis variation range is wider than that of a-axis, we can infer that the charge variation is mostly accomodated along the direction orthogonal to the layer planes, producing a volume increase at increasing charge content (Figure 3c).

Mode frequencies. We now analyse how the frequencies associated to the sliding and compressive modes vary at different charge content (Figure 4 and Figure 5). At $q = 0$, the sliding modes are Γ(4-7), Γ(8-9), A(1-4), A(7-10), while the compressive modes are Γ(10-11), Γ(12), A(5-6), A(11-12), where we grouped the modes with degenerate frequencies. We want here to notice that, according to the usual convention, the IBZ A point relative to the hexagonal space group 194 corresponds to the Z point of the IBZ relative to the space groups 63, 40, 15, 8, 5, 2 and 1, and to the Y point of the IBZ relative to the space groups 12 and 6; all the three A, Y and Z high symmetry points correspond to the direction $(0,0,1/2)$ of the respective reciprocal lattice. However, the displacement pattern of the A(1-12) modes is equivalent to that of the Z(1-12) and Y(1-12) modes; for this reason, we will simplify the notation by referring to the Z(1-12) and Y(1-12) modes as A(1-12) modes without any ambiguities. As expected, the loss of charge neutrality and the consequent symmetry reduction produce, in general, the split of some degenerate modes. Irrespective of the chemical composition, the frequencies of the considered modes are globally increasing at increasing q. However, the frequency-charge relation is not symmetric about $q = 0$: while for $q < 0$ the trend is smooth, for $q > 0$ sudden jumps are observed. Some of the jumps are expected due to a change in the space group; in other cases, frequency jumps are observed despite no variation of the system symmetries occurs. In this respect, the frequency-charge-stucture relation is not trivial and other descriptors must be considered to harness the frequency change at variable charge content.

Distortion mode analysis. Interplay between charges and structural distortions have already been observed in several classes of materials.[16,31,32] To analyse the details of the symmetry reduction upon removal of charge neutrality, we perform a group theoretical analysis of the charged structures by decomposing the ground state geometries into irreducible representations of the corresponding high symmetry hexagonal $P6_3mmc$ phase, aided by the ISODISTORT software.[33] Strain distortions are mainly due to variation of the c axis length, which we discussed above; thus, from now on, we will only discuss the overall structural distortion δ generated by pure atomic displacement (Figure 6). The main kind of distortion is Γ1+, corresponding to the bending of the X-M-X intralayer angle (Figure 7a); other distortions have negligible values, being 3 order of magnitude smaller. In few particular cases, such smaller distortions are not negligible and contribute to the overall atomic displacements in such a way to produce sudden variations of the atomic displacements (Figure 6). Such cases are: *i*) Γ5+, relative rigid sliding of adjacent MX_2 layers in MoSe at $q = 0.1$, WSe at $q = 0.2, 0.5, 0.7$, MoTe and WTe at $q = 1.0$ (Figure 7b); *ii*) Γ6+, intralayer rigid sliding of S planes with respect to W planes in WS system at $q = 0.7$ (Figure 7c).

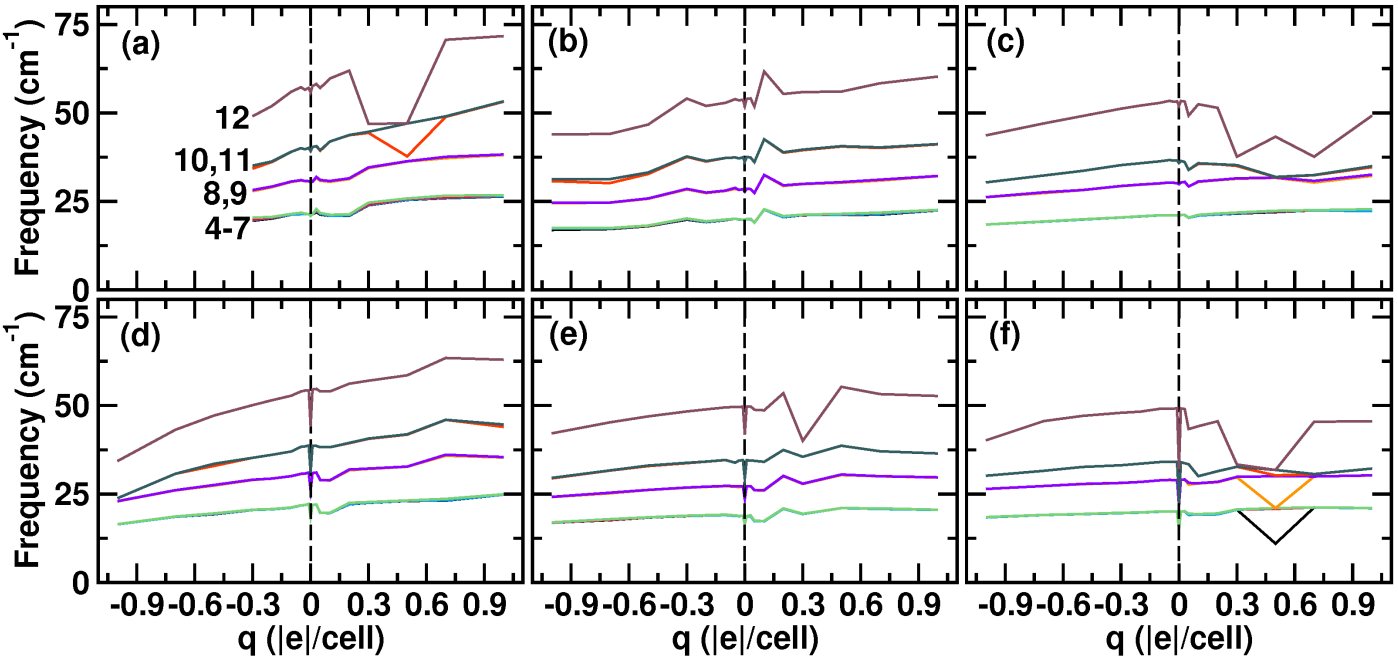

Fig. 4 Frequency of the phonon modes in branches 4-12 at the IBZ Γ point as a function of the system charge: (a) MoS, (b) MoSe, (c) MoTe, (d) WS, (e) WSe and (f) WTe systems. For clarity, we only show the lines connecting the data points, and omit the corresponding symbols.

Comparing Figure 6 with Figure 3c, it is possible to notice that such smaller distortions produce local minima in the volume-charge relation. Interestingly, the appearance of such extra distortions, then of sudden jumps in the $\delta(q)$ trend, does not induce a change of the crystallographic space group (see Table 1). For this reason, the analysis of the electronic structure is needed in order to clarify the relation between the charge content and the structural distortions, hence the frequency of the modes.

At fixed X anion, structural distortions are larger in WX than in MoX compounds, with some exceptions at specific q values of the MSe systems. This means that MoX systems are able to accomodate charge variations better than WX systems, limiting atomic displacements at the minimum. Similarly to what observed in the frequency-charge relation, δ values are not symmetric about $q = 0$. Distortions at $-|q|$ are lower than the corresponding ones at $+|q|$, and increase for $q > 0$; for $q < 0$, structural distortions decrease at increasing charge content in WX systems, while they increase at a lower rate in MoX systems. This outcome is a further example of the non-trivial charge-structure relation, and point out that multiple descriptors must be used to control the electro-structural coupling and its effect on the sliding-related vibrational modes of the system.

Electro-structural coupling. We now proceed with the study of the details of the electronic distribution. To this aim, we first perform a charge Bader analysis in all the considered systems, and consider the difference $q_B = q_M - q_X$, where q_M and q_X are the Bader charges of the X and M atomic species, respectively (Figure 8a); we then calculate the $C_{M,X}$ M-X bond covalency[34] and the C_{ph}(M-X) cophonicity[20] of the M-X pair, in the range $[-10, 0]$ eV and $[0, 75]$ cm^{-1}, respectively (Figure 8b-c). The M-X pair cophonicity is a measure of how the M and X atomic species contribute to form the phonon states in the considered range, and has been applied to the study of the electro-structural coupling in distinct classes of materials.[35–37] We observe that the variation range of q_B is wider in WX systems, and can be put in correspondance with a larger variation of the structural distortions with the charge content (Figure 6). Bond covalency is slightly decreasing upon charge injection, displaying a general linear trend with the system charge; however, by comparing Figure 8b) and c), it is immediately apparent that the covalent character of the bond is not strictly related to the q_B charge difference, nor directly connected with the structural distortions δ (Figure 6). Similar observation can be applied to the cophonicity data: in a good approximation, C_{ph}(M-X) is linear with the charge content, after neglecting few local minima/maxima due to more subtle electronic features we will discuss later on. We also compute the electron localization function[38,39] (ELF) of all the considered systems. Irrespective of the chemistry and the charge content, no charge localization occurs in any specific volume of the system cell; this can be immediately appreciated by inspecting Figure 9, where we report the ELFs of selected WTe systems, as an example. These last outcomes suggest that the electronic and dynamic features of the ionic environment are the result of a delicate balance between local rearrangements of the electron density, structural distortions and overall charge neutrality perturbation. In this respect, we now focus on the subtle details of the electronic density spatial distribution by analysing the atomic orbital polarization.

Orbital polarization. The charge density can be partitioned in atom-centered hydrogen-like orbitals, so as to uncover the features of electronic flows through the structure at variable charge content q.[22] We then measure the orbital polarization[40,41] of the X and M atomic species in each of the relaxed systems. Orbital

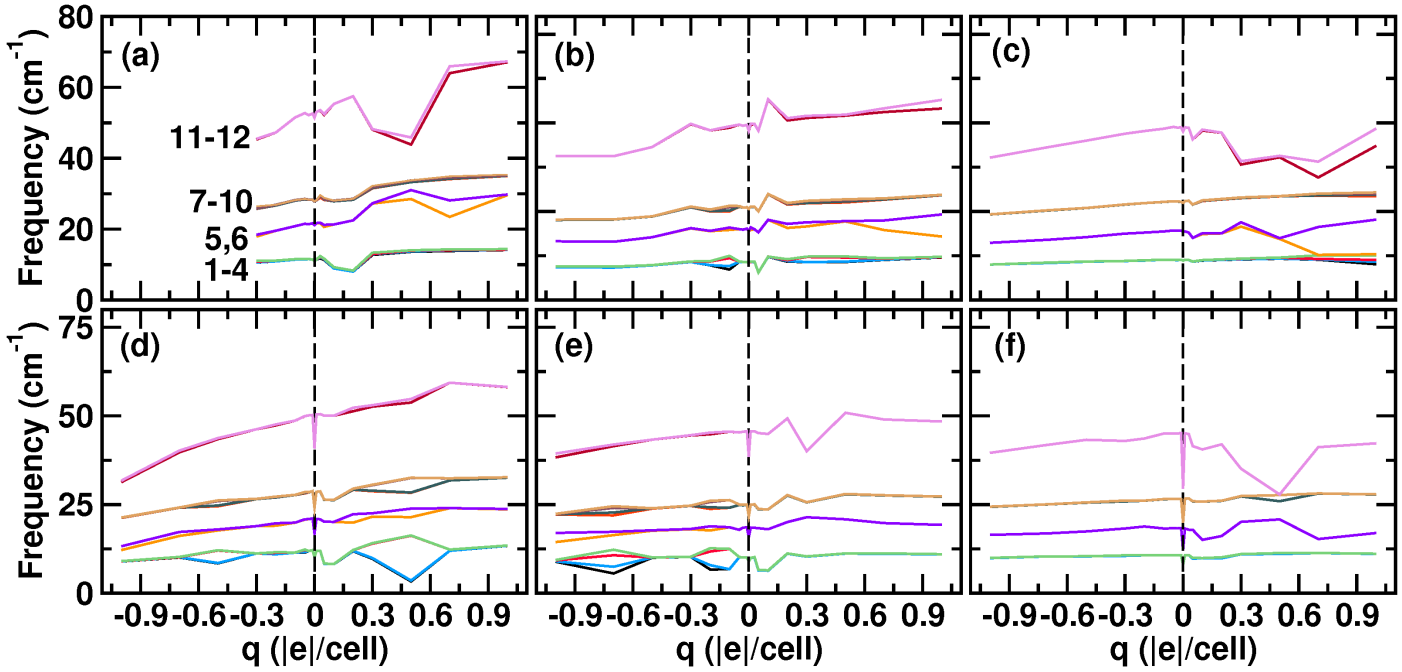

Fig. 5 Frequency of the phonon modes in branches 1-12 at the IBZ A point as a function of the system charge: (a) MoS, (b) MoSe, (c) MoTe, (d) WS, (e) WSe and (f) WTe systems. For clarity, we only show the lines connecting the data points, and omit the corresponding symbols.

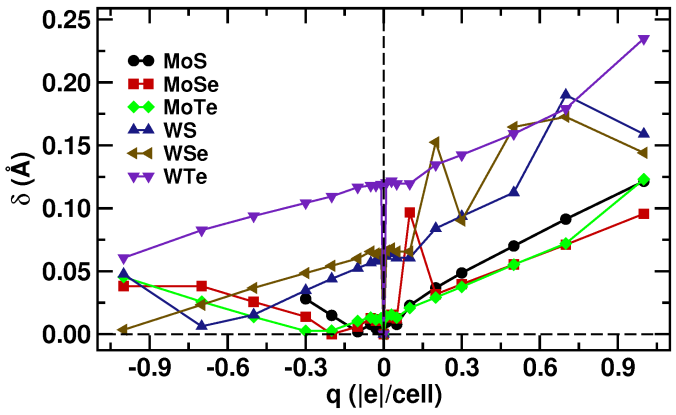

Fig. 6 Overall structural distortion δ as a function of the charge content q. Lines are guides for the eye.

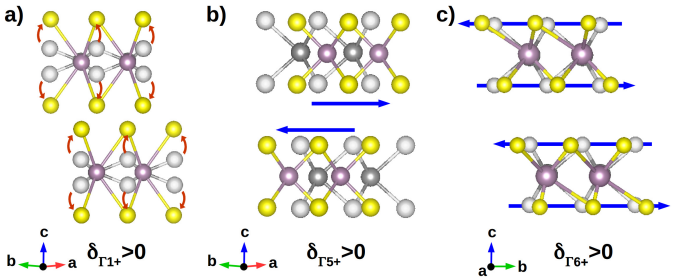

Fig. 7 Schematics of (a) Γ1+, (b) Γ5+ and (c) Γ6+ distortion modes corresponding to the bending of the X-M-X intralayer angle, rigid interlayer sliding, and intralayer rigid sliding of X planes relative M planes, respectively; positive distortion $\delta_{\Gamma 1+}$, $\delta_{\Gamma 5+}$ and $\delta_{\Gamma 6+}$ amplitudes indicate displacements along the directions shown by the arrows. Γ1+ distortion is dominant in all the examined cases. Atom color legend is the same as in Figure 1; grey spheres represent undistorted atomic positions. Displacements are magnified for clarity.

polarization $\mathscr{P}_{l_1 m_{l1}, l_2 m_{l2}}$ of the $|l_1 m_{l1}\rangle$ orbital relative to the $|l_2 m_{l2}\rangle$ orbital is defined as

$$\mathscr{P}_{l_1 m_{l1}, l_2 m_{l2}} = \frac{n_{l_1 m_{l1}} - n_{l_2 m_{l2}}}{n_{l_1 m_{l1}} + n_{l_2 m_{l2}}}, \quad (1)$$

where $n_{l_1 m_{l1}}$ and $n_{l_2 m_{l2}}$ are the occupancies of $|l_1 m_{l1}\rangle$ and $|l_2 m_{l2}\rangle$ orbitals, with orbital quantum number l_i and magnetic quantum number m_{li}, respectively. It measures the charge excess of the former orbital with respect to the latter: positive (negative) values indicate that m_{l1} orbital is more (less) populated than m_{l2} orbital. In the considered cases, the observed local maxima and minima of $\mathscr{P}(q)$ do not appear to be related to a change of the space group, the latter, instead, determining the frequency split/degeneracy (Figure 10).

In all charged systems, X p_x and p_y orbitals are almost equally populated (Figure 10a), with an exception at $q = \pm 0.03$ for all the systems and at $q = 0.01$ for the MoSe system, where p_x orbital is more populated than the p_y one. On the other hand, p_z orbital displays an excess of population with respect to both p_x and p_y orbitals (Figure 10b-c). At fixed M cation, $\mathscr{P}_{p_x,p_z}$ and $\mathscr{P}_{p_y,p_z}$ polarizations increase as MTe < MS < MSe, assuming higher values if M=W. The t_{2g} orbitals are more populated than the e_g ones (Figure 10d), with $d_{3z^2-r^2}$ orbital bearing an excess of charge with respect to the $d_{x^2-y^2}$ orbital (Figure 10e). In general, at fixed M cation and charge content q, the $d_{3z^2-r^2}$ population decreases with the X species as S>Se>Te, whereas higher population is found in WX systems (Figure 10e). The amount with which the $d_{3z^2-r^2}$ orbital can accommodate a specific amount of charge is therefore determined by both the M and X atomic types. By comparing

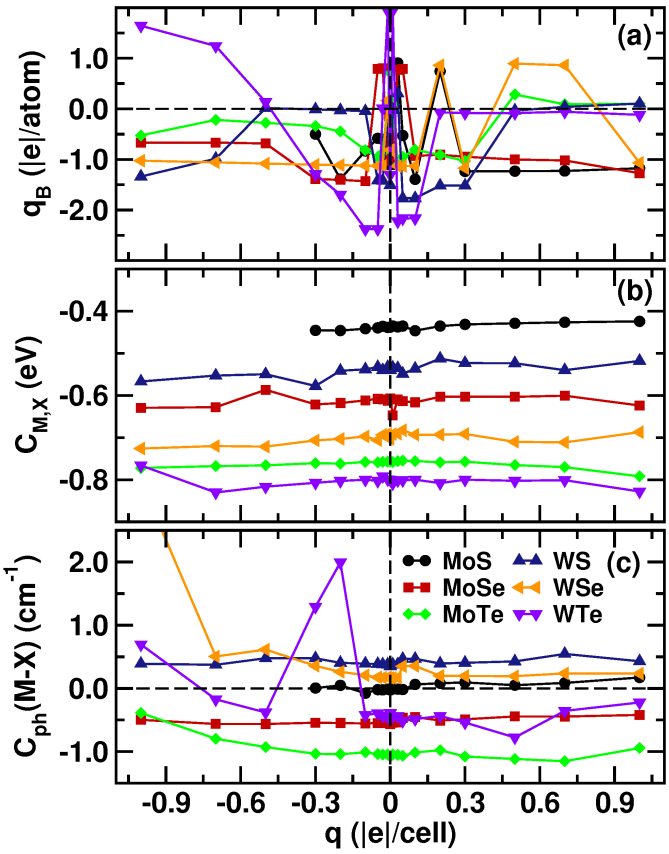

Fig. 8 (a) q_B Bader charge difference ($|e|/atom$), (b) $C_{M,X}$ M-X bond covalency (eV) and (c) C_{ph}(M-X) cophonicity (cm^{-1}) of the M-X pair as a function of the system charge q. For clarity, in plot (c) we do not show the C_{ph}(W-Se) $= 3.28$ cm^{-1} value at $q = -1.0$. Lines are guides for the eye.

Figure 10d) and e), it is possible to appreciate that, upon charge injection, a flow of charge occurs from the t_{2g} to the e_g orbitals, in particular towards the $d_{3z^2-r^2}$ one, which results to be more prone to accomodate the incoming electrons. We can therefore infer that this mechanism accounts for the c-axis variation with the system charge q. In this respect, ion substitution regulates the charge transfer from the planes parallel to the xy-plane and containing the X anions towards an axis parallel to the $\hat{c}$ direction, with the $\mathscr{P}_{t2g,eg}$ orbital polarization being the quantity controlling such transfer. Moreover, $\mathscr{P}_{t2g,eg}$ regulates the M-X interaction, hence the lattice dynamics. Following these results, we continue our analysis by relating the frequency of the considered Γ and A modes to the $\mathscr{P}_{t2g,eg}$ orbital polarization values calculated at the same system charge (Figure 11 and Figure 12). In order to better understand what is the relation between the frequencies and the orbital polarization, we first focus on the considered Γ(4-12) modes (Figure 11) and calculate the average frequency ω at fixed $\mathscr{P}_{t2g,eg}$ value, thus obtaining a $\{\omega, \mathscr{P}_{t2g,eg}\}$ data set for each MX system; we then evaluate the linear interpolation of such data sets and report the results in Figure 13a. We repeat the same procedure on the A(1-12) modes and show the interpolated data in Figure 13b. An inspection of the aforementioned figures clearly show that the mode frequencies overall increase with the $\mathscr{P}_{t2g,eg}$ orbital polarization. By controlling the $\mathscr{P}_{t2g,eg}$ orbital polarization, it is then possible to finely tune the considered phonon modes relative to layer sliding; to this aim, we will exploit the connection between $\mathscr{P}_{t2g,eg}$ with the M–X bond covalency and cophonicity. Irrespective of the chemical composition, at a fixed charge, $\mathscr{P}_{t2g,eg}$ is decreasing with increasing $C_{M,X}$ and C_{ph}(M-X) (Figure 14), the latter two descriptors being connected with the atomic type, the structural distortions and the electronic density distribution, as we have already shown in previous studies.[20–22] In this respect, such quantities capture several entangled properties that can be singularly adjusted to finely tune the covalency and cophonicity values. Chemical composition and stoichiometry can be chosen in such a way so as to induce specific structural distortions that alter the electronic distribution and are more suitable to accomodate a specific amount of charge in the structure; at the same time, they alter the interatomic interactions that determine the vibrational motions of the system. We can thus conclude that covalency and cophonicity can be used as a knob to control the $\mathscr{P}_{t2g,eg}$ orbital polarization, and hence low-frequency phonons contributing to intrisic friction in charged MX_2 systems.

Conclusions

We studied how the presence of non-null electronic charge affects the low-frequency modes influencing intrinsic friction in layered transition metal dichalcogenides. We find that any deviation from charge neutrality results in complex rearrangements of the electronic density and atomic positions, inducing electronic and structural transitions. Charge injection determines an expansion of the cell volume thanks to accumulation of charge along an axis orthogonal to the MX_2 layers. Such accumulation is accounted by the $d_{3z^2-r^2}$ orbital of the transition metal and it is regulated by the $\mathscr{P}_{t2g,eg}$ orbital polarization; the latter also determines the M-X interactions, hence the modes affecting the intrinsic friction. The frequencies of such modes increase with the $\mathscr{P}_{t2g,eg}$ orbital polarization. In turn, increasing bond covalency and cophonicity induce a decrease of the $\mathscr{P}_{t2g,eg}$ orbital polarization at a fixed charge content. With suitable choice of the atomic type, it is possible to control such electro-structural descriptors, then the orbital polarization and the mode frequency. Such relations are the result of subtle electro-vibrational coupling. Electron-phonon coupling can thus be exploited to control the vibrational frequencies of the system: by tuning the cophonicity and covalency values, we can finely control charge flow through atomic orbitals hence the vibrational frequencies at specific charge content. This feature can be exploited to finely tune intrinsic friction to facilitate assembly and operation of nanoelectromechanical systems and, ultimately, to control the electronic charge distribution in TMD-based devices for application beyond nanoscale tribology. The information gained with the present study will be extended in future works, where we will investigate the role of Coulombic forces arising from charge displacement and localization during tribological conditions.

Ackowledgements

This work has been done with the support of the Czech Science Foundation, project 17-24164Y. This work was sup-

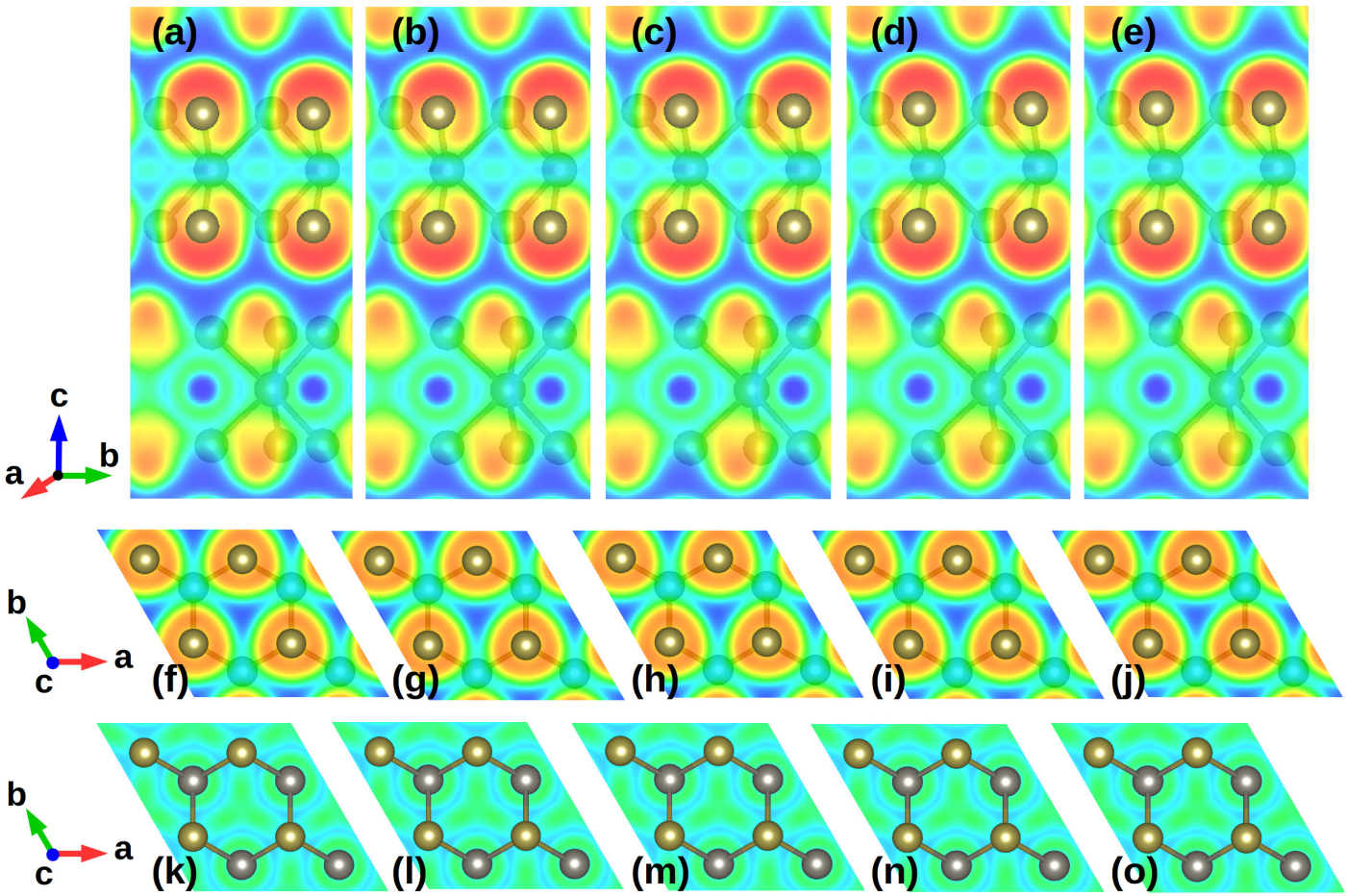

Fig. 9 Electron localization function (ELF) surfaces of the WTe systems calculated at (a,f,k) $q = -1.0$, (b,g,l) $q = -0.5$, (c,h,m) $q = 0.0$, (d,i,n) $q = 0.5$, and (e,j,o) $q = 1.0\ |e|/atom$, respectively. Surfaces have been obtained by projecting the corresponding ELFs onto (a-e) (100) plane containing Te atoms, (f-j) (001) plane containing Te atoms, and (k-o) (001) plane containing W cations, respectively. RGB gradient represents the charge localization, where red color corresponds to the highest ELF value. Orientation of the crystallographic axes, reported on the left-side of the figure, are shared among the (a-e), (f-j) and (k-o) subfigures, respectively.

ported by the IT4Innovations Centre of Excellence project (CZ.1.05/1.1.00/02.0070), funded by the European Regional Development Fund and the national budget of the Czech Republic via the Research and Development for Innovations Operational Programme, as well as Czech Ministry of Education, Youth and Sports via the project Large Research, Development and Innovations Infrastructures (LM2011033).

References

1 B. Persson, *Sliding Friction: Physical Principles and Applications*, Springer-Verlag Berlin Heidelberg, 2000.

2 E. Gnecco, R. Bennewitz, T. Gyalog and E. Meyer, *Journal of Physics: Condensed Matter*, 2001, **13**, R619.

3 A. Vanossi, N. Manini, M. Urbakh, S. Zapperi and E. Tosatti, *Rev. Mod. Phys.*, 2013, **85**, 529–552.

4 S. Cahangirov, C. Ataca, M. Topsakal, H. Sahin and S. Ciraci, *Phys. Rev. Lett.*, 2012, **108**, 126103.

5 T. Onodera, Y. Morita, A. Suzuki, M. Koyama, H. Tsuboi, N. Hatakeyama, A. Endou, H. Takaba, M. Kubo, F. Dassenoy, C. Minfray, L. Joly-Pottuz, J.-M. Martin and A. Miyamoto, *J. Phys. Chem. B*, 2009, **113**, 16526–16536.

6 T. Onodera, Y. Morita, R. Nagumo, R. Miura, A. Suzuki, H. Tsuboi, N. Hatakeyama, A. Endou, H. Takaba, F. Dassenoy, C. Minfray, L. Joly-Pottuz, M. Kubo, J.-M. Martin and A. Miyamoto, *J. Phys. Chem. B*, 2010, **114**, 15832.

7 T. Liang, W. G. Sawyer, S. S. Perry, S. B. Sinnott and S. R. Phillpot, *Phys. Rev. B*, 2008, **77**, 104105.

8 Y. Morita, T. Onodera, A. Suzuki, R. Sahnoun, M. Koyama, H. Tsuboi, N. Hatakeyama, A. Endou, H. Takaba, M. Kubo, C. A. D. Carpio, T. Shin-yoshi, N. Nishino, A. Suzuki and A. Miyamoto, *Appl. Surf. Sci.*, 2008, **254**, 7618 – 7621.

9 B. J. Irving, P. Nicolini and T. Polcar, *Nanoscale*, 2017, **9**, 5597–5607.

10 P. Nicolini and T. Polcar, *Computational Materials Science*, 2016, **115**, 158 – 169.

11 L. B. Loeb, *Science*, 1945, **102**, 573–576.

12 T. A. L. Burgo, C. A. Silva, L. B. S. Balestrin and F. Galembeck, 2013, **3**, 2384 EP –.

13 A. Diaz and R. Felix-Navarro, *Journal of Electrostatics*, 2004, **62**, 277 – 290.

14 F. R. Fan, W. Tang and Z. L. Wang, *Advanced Materials*, 2016, **28**, 4283–4305.

15 J. P. Oviedo, S. KC, N. Lu, J. Wang, K. Cho, R. M. Wallace and M. J. Kim, *ACS Nano*, 2015, **9**, 1543–1551.

16 M. Chhowalla, H. S. Shin, G. Eda, L.-J. Li, K. P. Loh and H. Zhang, *Nat. Chem.*, 2013, **5**, 263–275.

17 J. P. Perdew, K. Burke and M. Ernzerhof, *Phys. Rev. Lett.*, 1996, **77**, 3865–3868.

18 (*a*) G. Kresse and J. FurthmÃijller, *Comp. Mater. Sci.*, 1996, **6**, 15 – 50; (*b*) G. Kresse and D. Joubert, *Phys. Rev. B*, 1999, **59**, 1758–1775.

19 S. Grimme, *J. Comp. Chem.*, 2006, **27**, 1787–1799.

20 A. Cammarata and T. Polcar, *Inorg. Chem.*, 2015, **54**, 5739–5744.

21 A. Cammarata and T. Polcar, *RSC Adv.*, 2015, **5**, 106809–106818.

22 A. Cammarata and T. Polcar, *Phys. Chem. Chem. Phys.*, 2016, **18**, 4807–4813.

23 B. Schönfeld, J. J. Huang and S. C. Moss, *Acta Crystallogr. B*, 1983, **39**, 404–407.

24 V. Kalikhman, *Inorg. Mater.*, 1983, **19**, 957–962.

25 L. Brixner, *J. Inorg. Nucl. Chem.*, 1962, **24**, 257 – 263.

26 W. Schutte, J. D. Boer and F. Jellinek, *J. Solid State Chem.*, 1987, **70**, 207 – 209.

27 V. L. Kalikhman, *Neorganicheskie Materialy*, 1983, **19**, 1060 – 1065.

28 A. A. Yanaki and V. A. Obolonchik, *Inorg. Mater.*, 1973, **9**, 1855–1858.

29 A. Togo, F. Oba and I. Tanaka, *Phys. Rev. B*, 2008, **78**, 134106.

30 W. Setyawan and S. Curtarolo, *Comp. Mater. Sci*, 2010, **49**, 299 – 312.

31 F. Flicker and J. van Wezel, *Nat Commun*, 2015, **6**, 7034.

32 A. Cammarata and J. M. Rondinelli, *Applied Physics Letters*, 2016, **108**, 213109.

33 B. J. Campbell, H. T. Stokes, D. E. Tanner and D. M. Hatch, *J. Appl. Cryst.*, 2006, **39**, 607–614.

34 A. Cammarata and J. M. Rondinelli, *J. Chem. Phys.*, 2014, **141**, 114704.

35 Z. Lu, C. Chen, Z. M. Baiyee, X. Chen, C. Niu and F. Ciucci, *Phys. Chem. Chem. Phys.*, 2015, **17**, 32547–32555.

36 T. Hu, M. Hu, Z. Li, H. Zhang, C. Zhang, J. Wang and X. Wang, *J. Phys. Chem. A*, 2015, **119**, 12977–12984.

37 R. Fei, W. Kang and L. Yang, *Phys. Rev. Lett.*, 2016, **117**, 097601.

38 A. D. Becke and K. E. Edgecombe, *J. Chem. Phys.*, 1990, **92**, 5397–5403.

39 A. Savin, O. Jepsen, J. Flad, O. K. Andersen, H. Preuss and H. G. von Schnering, *Angewandte Chemie International Edition in English*, 1992, **31**, 187–188.

40 A. Cammarata and J. M. Rondinelli, *Phys. Rev. B*, 2013, **87**, 155135.

41 M. J. Han, C. A. Marianetti and A. J. Millis, *Phys. Rev. B*, 2010, **82**, 134408.

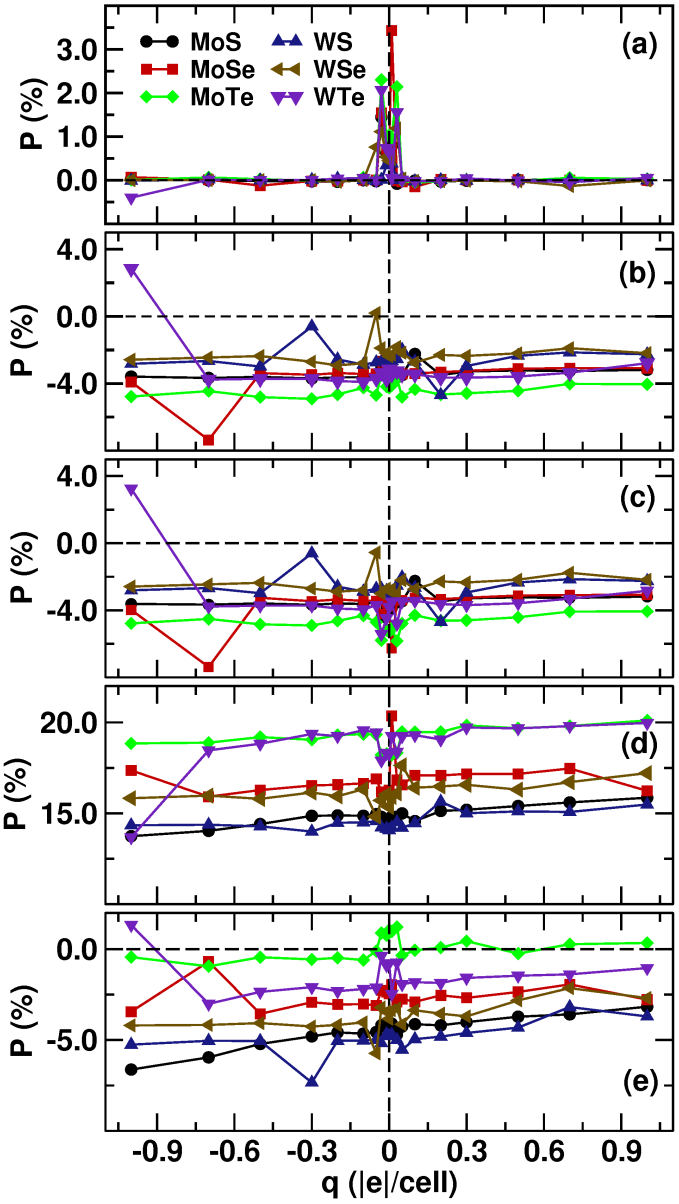

Fig. 10 Orbital polarization as a function of the system charge q: (a) X $\mathscr{P}_{px,py}$, (b) X $\mathscr{P}_{px,pz}$, (c) X $\mathscr{P}_{py,pz}$, (d) M $\mathscr{P}_{t2g,eg}$, (e) M $\mathscr{P}_{d_{x^2-y^2},d_{3z^2-r^2}}$. Upon charge injection, the population of the M $d_{3z^2-r^2}$ orbital increases, accounting for the variation of the c lattice parameter. Lines are guides for the eye.

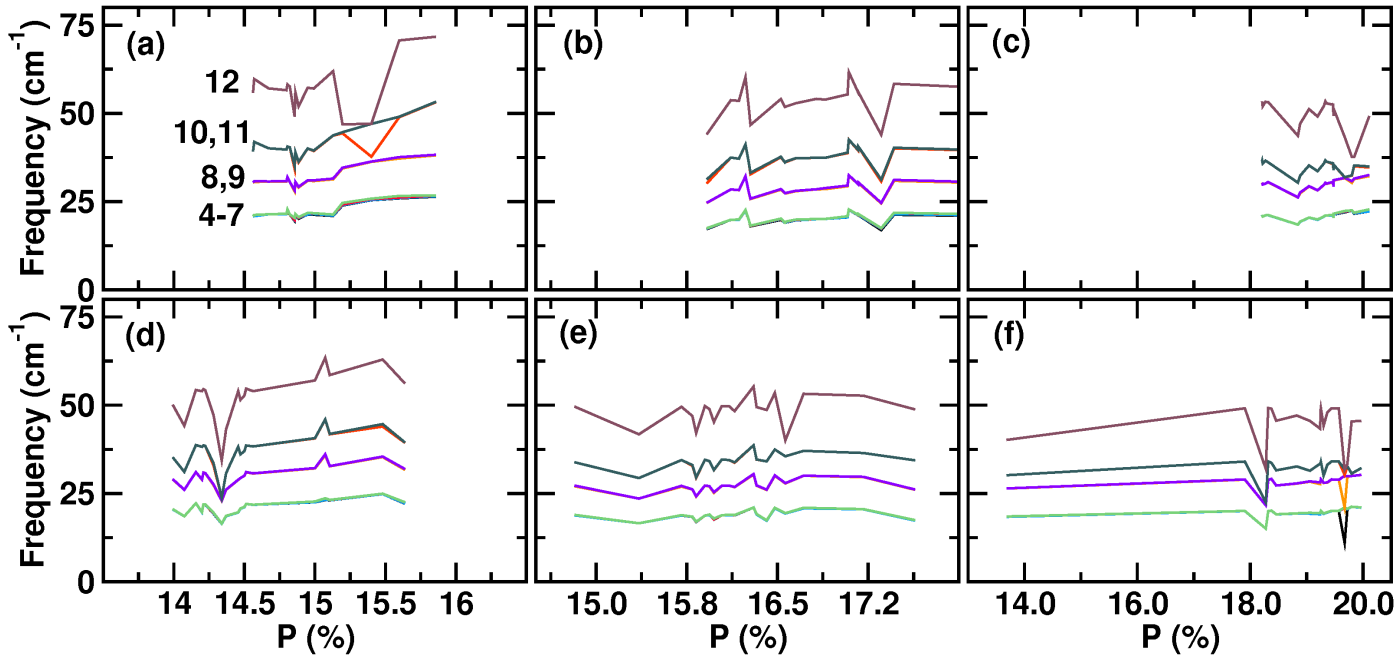

Fig. 11 Frequency of the phonon modes in branches 4-12 at the IBZ Γ point as a function of M $\mathscr{P}_{t2g,eg}$ orbital polarization of (a) MoS, (b) MoSe, (c) MoTe, (d) WS, (e) WSe and (f) WTe systems. For clarity, we only show the lines connecting the data points, and omit the corresponding symbols.

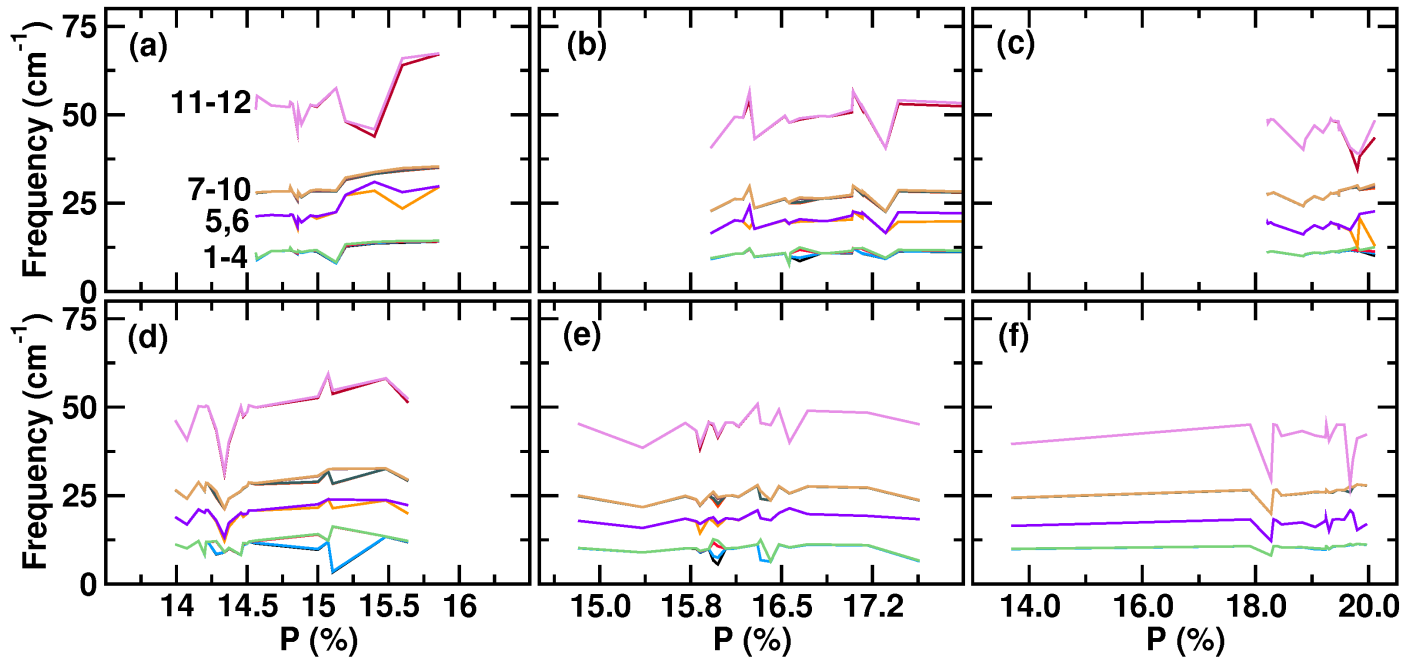

Fig. 12 Frequency of the phonon modes in branches 1-12 at the IBZ A point as a function of M $\mathscr{P}_{t2g,eg}$ orbital polarization of (a) MoS, (b) MoSe, (c) MoTe, (d) WS, (e) WSe and (f) WTe systems. For clarity, we only show the lines connecting the data points, and omit the corresponding symbols.

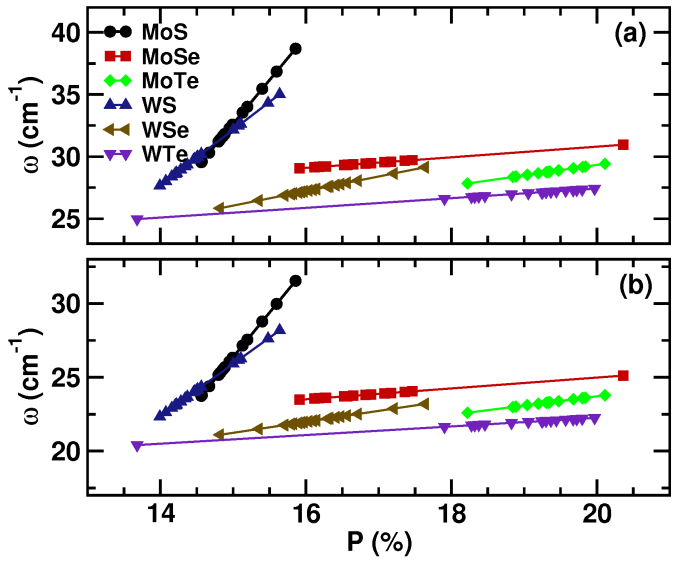

Fig. 13 Linear interpolation of the average frequency ω as a function of the $\mathscr{P}_{t2g,eg}$ orbital polarization of the considered (a) Γ(4-12) and (b) A(1-12) phonon modes, respectively. Irrespective of the chemical composition, mode frequencies are overall increasing with increasing $\mathscr{P}_{t2g,eg}$ orbital polarization.

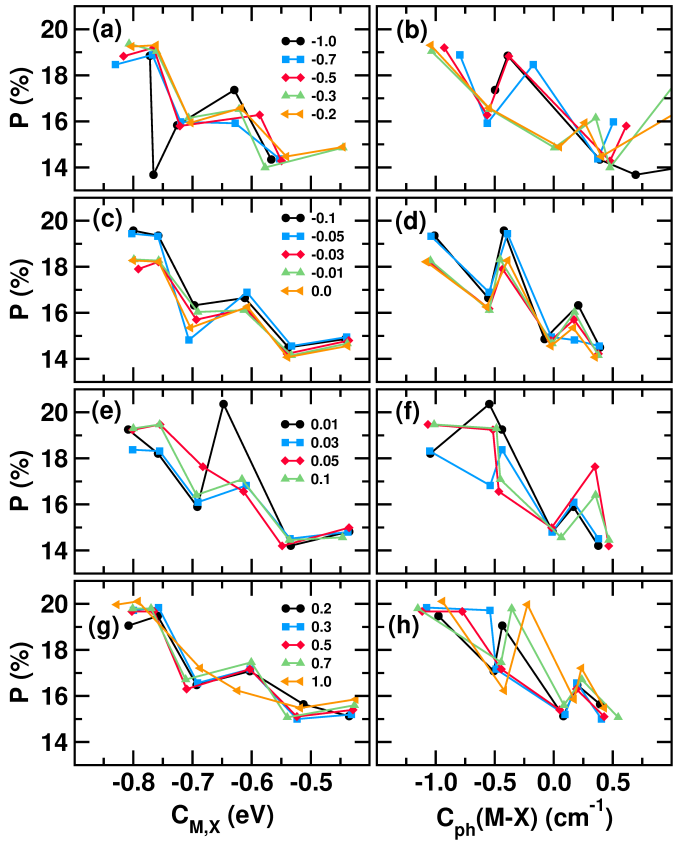

Fig. 14 M-cation $\mathscr{P}_{t2g,eg}$ orbital polarization as a function of (a,c,e,g) M-X bond covalency and (b,d,f,h) M-X pair cophonicity. Plots (a) and (b), (c) and (d), (e) and (f), (g) and (h) share the same legend which refers to the charge content of the system. In plot (b), values at C_{ph}(M-X) > 0.5 cm^{-1} are not shown for clarity. Lines are guides for the eye.